





Generating bright-field images of stained tissue slices from Mueller matrix polarimetric images with CycleGAN using unpaired dataset

Jiahao Fan ^{*}, Nan Zeng^{*}, Honghui He ^{*,§}, Chao He ^{†,¶},
Shaoxiong Liu[‡] and Hui Ma ^{*}

**Shenzhen Key Laboratory for Minimal Invasive Medical Technologies
Guangdong Research Center of Polarization Imaging and
Measurement Engineering Technology Institute of Biopharmaceutical and
Health Engineering, Tsinghua Shenzhen International Graduate School
Tsinghua University, Shenzhen 518055, P. R. China*

*†Department of Engineering Science
University of Oxford, Oxford, UK*

*‡Shenzhen Sixth People's Hospital (Nanshan Hospital)
Huazhong University of Science
and Technology Union Shenzhen Hospital
Shenzhen 518052, P. R. China*

§he.honghui@sz.tsinghua.edu.cn

¶chao.he@eng.ox.ac.uk

Received 27 November 2023

Accepted 29 January 2024

Published 9 March 2024

Recently, Mueller matrix (MM) polarimetric imaging-assisted pathology detection methods are showing great potential in clinical diagnosis. However, since our human eyes cannot observe polarized light directly, it raises a notable challenge for interpreting the measurement results by pathologists who have limited familiarity with polarization images. One feasible approach is to combine MM polarimetric imaging with virtual staining techniques to generate standardized stained images, inheriting the advantages of information-abundant MM polarimetric imaging. In this study, we develop a model using unpaired MM polarimetric images and bright-field images for generating standard hematoxylin and eosin (H&E) stained tissue images. Compared with the existing polarization virtual staining techniques primarily based on the model training with paired images, the proposed Cycle-Consistent Generative Adversarial Networks (CycleGAN)-based model simplifies data acquisition and data preprocessing to a great extent. The outcomes demonstrate the feasibility of training CycleGAN with unpaired polarization images and their

[§]Corresponding author.

This is an Open Access article. It is distributed under the terms of the Creative Commons Attribution 4.0 (CC-BY) License. Further distribution of this work is permitted, provided the original work is properly cited.

corresponding bright-field images as a viable approach, which provides an intuitive manner for pathologists for future polarization-assisted digital pathology.

Keywords: Polarization imaging; Mueller matrix; virtual staining; digital pathology; CycleGAN.

1. Introduction

As a non-invasive and non-contact method, polarization imaging can offer rich structural and optical information of biomedical samples label-freely.^{1–8} In biomedical studies, we often use Stokes vectors^{9,10} to describe the polarization states of incident and output light. The Stokes vector of light can be represented as $S = (S_1, S_2, S_3, S_4)^T$. Hence, a Mueller matrix (MM) can be used to describe the polarization modulation ability of a sample. The relationship between Stokes vector and MM can be represented as $S_{\text{out}} = MS_{\text{in}}$, where S_{out} and S_{in} are the Stokes vectors of the output and incident light, and M is the MM of the sample. Thus, all the polarization-related properties, namely depolarization, dichroism and birefringence of tissue samples can be represented by MM, which contains abundant structural information useful for clinical trials. Recently, MM polarization imaging-assisted pathology detection methods have shown great potential in clinical diagnosis.^{11,12} By analyzing the MM-derived polarimetric parameters, we can quantitatively assess the structural features of skin tissue,¹³ liver tissue,¹⁴ breast tissue,¹⁵ colon tissue,^{16–20} cervical tissue,^{21,22} and more. However, since our human eyes cannot observe polarized light directly, it raises a notable challenge for interpreting the measurement results by pathologists who have limited familiarity with polarization images. Therefore, finding a way to present the MM polarimetric results intuitively for pathologists is a critical issue for future polarization-assisted digital pathology.

Currently, the “gold standard” of pathological diagnosis is the microscopic observation and evaluation of histological tissue sections stained with dyes such as hematoxylin and eosin (H&E).²³ In addition, virtual staining technology has experienced rapid development in recent years.²⁴ This technology refers to the use of computer image processing and analysis methods to virtually stain pathological tissue slice images, thereby bypassing the general chemical staining process. For instance, Rivenson *et al.* successfully achieved the application of virtual staining of unlabeled tissue samples using

autofluorescence images through deep learning.²⁵ In addition, quantitative phase imaging (QPI) based on the refractive index distribution of stained biological samples has also been used for virtual staining. Rivenson *et al.* utilized quantitative phase images of various unlabeled tissue slices and transformed them into virtual H&E, Jones, and Masson’s trichrome (MT) staining using convolutional neural networks.²⁶ Thus, one feasible approach is to combine MM polarization imaging with virtual staining techniques to transform full-polarization images into standardized stained images. This polarization virtual staining technique inherits the advantages of MM polarimetric imaging, while integrating the interpretability and clinical acceptability of pathological staining methods. From such an idea, the existing polarization virtual staining techniques are primarily based on the model training with paired images, requiring the acquisition of polarization images and bright-field images from the same tissue sample area with sub-pixel-level registration. For instance, Si *et al.* proposed a paired virtual staining scheme to convert full-polarization images of human breast and liver tissue slices into H&E-stained images.²⁷ However, the model training with paired images brings great challenges in data acquisition and preprocessing. In this study, we develop a model using unpaired MM polarization images and bright-field images for generating standard H&E-stained tissue images. The proposed Cycle-Consistent Generative Adversarial Networks (CycleGAN)-based model simplifies data acquisition and data preprocessing, because we no longer have to collect a large number of polarization images and bright-field images of the same area of tissue slices with pixel-level registration, which also eliminates the need for subsequent image registration work. We separately obtain the unpaired MM polarization images and bright-field images of human intestinal tissue sections. After obtaining the raw image data, we conduct dimensionality reduction on the MM polarization images and stain normalization on the bright-field images, along with image cropping to augment the dataset. This data preprocessing

provides a high-quality dataset for the CycleGAN model training. After the model training, we select several regions in the samples for both polarization and bright-field imaging. Image registration algorithms are applied to align the polarization and bright-field images, utilized for evaluating the model's performance. The outcomes demonstrate the feasibility of training CycleGAN with unpaired polarization images and their corresponding bright-field images as a viable approach.

2. Materials and Methods

2.1. MM imaging system and tissue samples

In this study, we used a transmission MM microscope based on dual-rotating retarders (DRR) method²⁸ to obtain polarization images. As shown in Fig. 1(a), a light beam emitted from an LED (633 nm, 30 W, Cree Inc., United States) is converged into parallel beam through a lens. The light beam then passes through a polarization state generator (PSG) consisting of a linear polarizer (P_2 , extinction ratio 1000:1, Daheng Optics, China) and a quarter-wave plate (R_2 , Daheng Optics, China), which is capable of modulating the polarization state of light. The polarized light then passes through the objective lens ($4 \times /0.1$ NA, UPlan-Sapo, Olympus, Japan) and a polarization state

analyzer (PSA), which also consists of a quarter-wave plate (R_1 , Daheng Optics, China) and a linear polarizer (P_1 , extinction ratio 1000:1, Daheng Optics, China), after interacting with the sample. The transmitted light is finally collected by the camera (MV-CA016-10 UM, 12-bit, Hikvision, China). In the MM imaging process, we fixed the axes of both polarizers P_1 and P_2 along the horizontal direction, and then rotated the two wave plates R_1 and R_2 with an angular speed ratio of $\omega_{R1} : \omega_{R2} = 5 : 1$. Finally, as shown in Fig. 1(b), we acquired 30 polarization images whose intensity series is a periodic signal with the wave plate axis direction as a variable. The intensity can be expanded as in the following equation:

$$I = \alpha_0 + \sum_{n=1}^{12} (\alpha_n \cos 2n\theta + \beta_n \sin 2n\theta), \quad (1)$$

where I denotes the light intensity, the Fourier coefficients α_n and β_n are the functions of the MM elements, and θ denotes the rotation angle of the wave plate R_1 . By calculating α_n and β_n , we are able to compute the MM of the sample as shown in Fig. 1(c). Prior to a measurement, the MM microscope underwent a calibration process using standard samples to guarantee that the maximum error for each component is within 1%.^{29,30} We also used a wide-field microscope with a magnification of $4 \times$ to perform bright-field imaging on H&E-stained

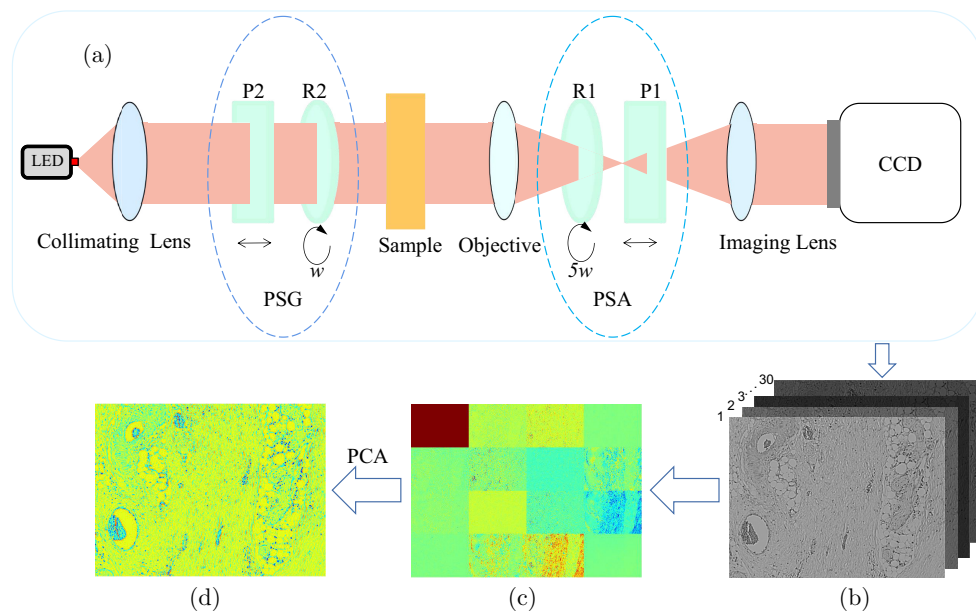


Fig. 1. Schematics of (a) transmission MM microscope based on DRR method; P: polarizer; R: quarter-wave plate. (b) 30 polarization grayscale images. (c) MM images and (d) PCA generated image based on MM.

tissue slices. Currently, more than 1000 human intestinal tissue slices were measured to produce both the bright-field and polarized images.

Here, we utilized nine human intestinal tissue slices provided by Shenzhen Sixth People’s Hospital (Nanshan Hospital) Huazhong University of Science and Technology Union Shenzhen Hospital. The tissue samples were prepared in the following process: they were initially formalin-fixed and paraffin-embedded, precisely sliced into $4\mu\text{m}$ thickness sections. Then, the sections were deparaffinized using xylene and carefully mounted onto standard glass slides. Finally, the deparaffined tissues were delicately stained with H&E before being covered with coverslips for preservation. This study was approved by the Ethics Committee of Tsinghua Shenzhen International Graduate School, Tsinghua University.

2.2. Data Preprocessing Methods

2.2.1. Principal component analysis for MM

The 16 MM elements essentially constitute 16 channels of a 2D image. In contrast, the 2D bright-field image of the sample contains only three channels. To effectively employ CycleGAN for the conversion of MM polarimetric images to bright-field images, it is imperative that the image dimensions between these two domains are aligned³¹ to ensure a uniformity in the image properties, including length, width, and the number of channels. Consequently, the high-dimensional MM needs to undergo a transformation to down-scale its dimensionality from 16 to 3. This modification is essential to maintain consistency in the channel numbers between MM and bright-field images.

To accomplish the dimensionality downscaling process while keeping the polarization information as much as possible, we adopted principal component analysis (PCA) on MM.³² PCA is a statistical method commonly used for dimensionality reduction. Its basic idea is to find the main variation directions of the data and project the data onto these directions to obtain a new set of uncorrelated features called principal components. Here, we used PCA to project the high-dimensional MM data into three-dimensional space to ensure that the number of channels matches the bright-field image while

maximizing the preservation of polarization information. First, we normalized the MM data to calculate the covariance matrix by PCA. Next, we obtained the eigenvalues and eigenvectors of the covariance matrix, which would become the new principal components. By selecting the first three eigenvectors with the largest eigenvalues, we achieved dimensionality reduction while retaining as much information as possible. Finally, we projected the original high-dimensional MM data into a three-dimensional space consisting of the selected principal components. Figure 1(d) shows the PCA-generated fusion image with three channels.

2.2.2. Stain normalization for bright-field images

For the staining process, variations in dye concentration and staining duration can influence staining outcomes. Besides, disparities in exposure time and other factors during the bright-field imaging process can also lead to variations in the hue of the images of stained tissue slices. Such hue disparities are not conducive to subsequent model training. Hence, there is a need of stain normalization for bright-field images to establish uniform staining characteristics across diverse images, ensuring consistency for both visual examination and computational analysis.³³ This entails modifying stain intensity, contrast, and color balance to enhance their suitability for analysis under consistent conditions.

In this study, we employed the “Vahadane” stain normalization algorithm on the bright field images of the H&E-stained tissue slices.³⁴ The algorithm encompasses the following steps:

- (1) Color space conversion: Initially, the algorithm transforms the raw pathology image from RGB color space to optical density (OD) color space. This conversion facilitates the separation of color information from luminance, enhancing the precision of color adjustments.
- (2) Generation of sample images: To train the stain normalization model, numerous small regions are randomly selected from the input image, and the color information from these regions serves as the basis for model training and is treated as source images within the color space.
- (3) Normalizing color distribution: Utilizing the OD color space, the algorithm scrutinizes the color distribution between source and target

images. It endeavors to identify a linear transformation that maps colors in the source image to the color distribution of the target image. This mapping is employed to fine-tune the source image's coloration.

- (4) Color Normalization: Building upon the generated color mapping, each pixel's color in the source image is adjusted to align with the target image concerning both color and brightness.
- (5) Color Inversion: Ultimately, the adjusted image is converted from OD color space back to RGB color space, yielding the final normalized image.

According to the above algorithm flow, we first selected a target image for stain normalization as shown in Fig. 2(a).

Subsequently, the source and target images were converted into another color space according to the following equation:

$$V = \ln \frac{I_0}{I}, \quad (2)$$

where I_0 is the value of light intensity passing through the unstained sample, which we denote as the pixel value in the RGB image. It is assumed that the light intensity does not change after passing through the unstained sample, and the pixel value in the RGB image is (255, 255, 255). I is the value of the light intensity after passing through and attenuated by the H&E-stained sample, i.e., the actual pixel value in the RGB image. V is the relative optical density matrix, which can be decomposed

into the product of the stain color appearance matrix W and the stain density matrix H according to the following equation:

$$V = W \times H, \quad (3)$$

here W denotes the effect of different staining dyes on the light absorption in the RGB channels, and H denotes the densities of different staining dyes in different pixels of the RGB image.

To achieve stain normalization, we initially separated the color space of the source and target images. We derived the relative optical density matrices for both of the source and target images according to Eq. (2). Subsequently, the objective function can be established as shown in the following equation:

$$F^* = \min_{W, H} \frac{1}{2} \|V - WH\|_F^2 + \lambda \sum_{j=1}^r \|H(j, :)\|_1, \quad (4)$$

$$W, H \geq 0, \|W(:, j)\|_2^2 = 1.$$

By minimizing the objective function, we obtained the matrices W and H . Then, by performing calculations on the matrix W_t of the target image and the matrix H_s^{norm} of the source image after the normalization, we acquired the relative optical density matrix V^{norm} for the normalized source image. Utilizing Eq. (2) in reverse, we derived the normalized RGB image. More details of the stain normalization process can refer to Ref. 34.

As depicted in Fig. 2(b), we successfully obtained the stain normalized bright-field images with a purplish hue, which is obviously different from the

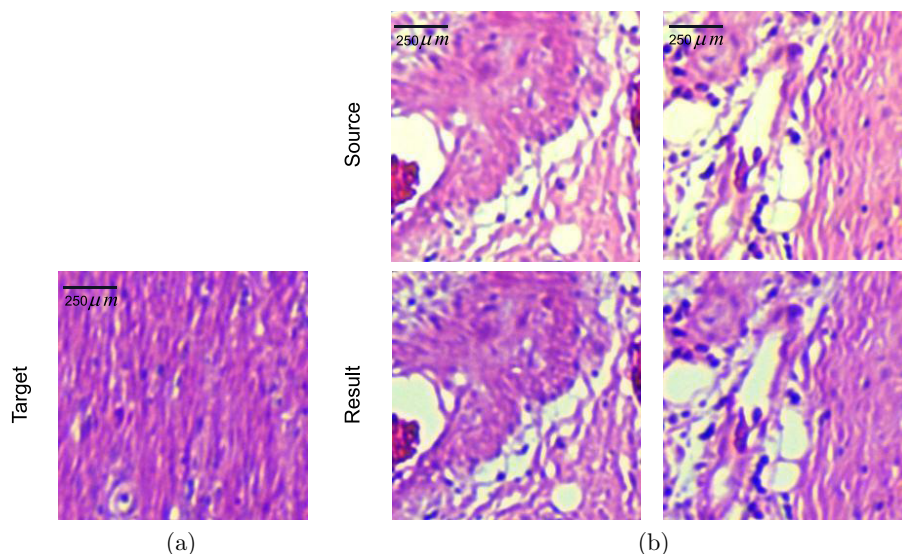


Fig. 2. (a) Target image for stain normalization. (b) Source images and results after stain normalization.

pinkish tone of the source image. This aligns more closely with the staining style of the target image, providing a high-quality dataset for the subsequent model training.

2.3. Image Conversion Methods

2.3.1. Cycle-consistent generative adversarial networks

CycleGAN is a deep learning model used for image translation and style transfer tasks.³⁵ It is an unsupervised learning method that can transform a set of images from one domain (Domain A) to another domain (Domain B) without the need for paired training data. The key idea behind CycleGAN is to achieve image translation through adversarial networks and cycle consistency loss. It can learn mappings between two domains. The core of CycleGAN consists of two generators and two discriminators, which compete with each other. The generators create realistic images, while the discriminators attempt to differentiate between generated images and real images. By introducing cycle consistency loss, CycleGAN ensures that the image translation from Domain A to Domain B and back to Domain A is reversible, enhancing the quality and consistency of generated images.

Here, for the image translation, we associated two imaging modalities: MM polarization images (denoted as x) and bright-field images (denoted as y). We employed the CycleGAN model for the mutual transformation between these two modalities. During the model training process, we selected an equal number of images from both the MM polarization image dataset and the bright-field image dataset. These images were fed into two generators, G_y and G_x . G_y and G_x are responsible for generating bright-field and MM polarization images, respectively. The images generated by both generators were then input to discriminators D_y and D_x . The discriminator D_y assesses whether the input image belongs to the real y -domain, while D_x evaluates if the input image is from the real x -domain.

For training the generators and discriminators, first we defined the adversarial loss function, as shown in the following equation:

$$\begin{cases} L_{\text{adv}}(G_x, D_x) = E_x[\log D_x(x)] + E_x[1 - \log D_x(G_x(y))], \\ L_{\text{adv}}(G_y, D_y) = E_y[\log D_y(y)] + E_y[1 - \log D_y(G_y(x))]. \end{cases} \quad (5)$$

For the conversion of x -domain images to generate y -domain images, discriminator D_y received both images generated by G_y and images from the real y -domain. We labeled the images generated by G_y as 0 and those from the real y -domain as 1. D_y then assigned a value between (0, 1) to the input images. Here, a value closer to 1 indicates a higher likelihood that the image belongs to the real y -domain, while a lower value suggests a higher likelihood that the image was generated by G_y . The above explanation also applies to the conversion of y -domain images to generate x -domain images. Next, we defined the cycle-consistency loss function, as shown in the following equation:

$$\begin{aligned} L_{\text{cycL1}}(G_x, G_y) \\ = E_x[\|G_x(G_y(x)) - x\|_1] + E_y[\|G_y(G_x(y)) - y\|_1]. \end{aligned} \quad (6)$$

The purpose of this loss function is to ensure that the images generated by the generator remain consistent and reversible during the process of moving from one domain to the other and back. Additionally, to guarantee structural consistency in the generated images during the cyclic process, we established a cycle structural consistency loss function,³⁶ as shown in the following equation:

$$\begin{aligned} L_{\text{cycSSIM}}(G_x, G_y) = E_x[\text{SSIM}(G_x(G_y(x)) - x)] \\ + E_y[\text{SSIM}(G_y(G_x(y)) - y)]. \end{aligned} \quad (7)$$

Last, we introduced an identity loss function as depicted in Eq. (8), to ensure that the generator maintains a certain level of consistency between the input and the output.

$$\begin{aligned} L_{\text{identity}}(G_x, G_y) \\ = E_x[\|G_x(x) - x\|_1] + E_y[\|G_y(y) - y\|_2]. \end{aligned} \quad (8)$$

Therefore, the total loss function can be defined as shown in the following equation:

$$\begin{aligned} \text{loss} = \lambda_1 L_{\text{adv}}(G_x, D_x) + \lambda_2 L_{\text{adv}}(G_y, D_y) \\ + \lambda_3 L_{\text{cycL1}}(G_x, G_y) + \lambda_3 L_{\text{cycSSIM}}(G_x, G_y) \\ + \lambda_4 L_{\text{identity}}(G_x, G_y), \end{aligned} \quad (9)$$

where λ represents the weights for various components of the loss function. Here, we set $\lambda_2 = 2\lambda_1$, emphasizing the generation of bright-field images.

2.3.2. Neural network architecture

Figure 3(a) illustrates the structure of the generator, which is an encoder-decoder network based on U-Net.³⁷ The initial input image is resized to a $256 \times 256 \times 3$ image and passes through a single convolution, resulting in a $256 \times 256 \times 64$ tensor. Two downsampling operations follow, reducing it to a $64 \times 64 \times 256$ tensor. Subsequently, nine layers of residual blocks are employed to extract features, and the tensor is restored to its original size through two upsampling operations. The final output image is generated after a convolution for the tensor. The skip-connection helps the model better preserve the original image structure and effectively prevents the problem of vanishing gradients during the training process.³⁸

Figure 3(b) provides an overview of the discriminator's architecture. The input image undergoes multiple convolution operations to extract features and subsequently goes through pooling, resulting in a reduction to a $1 \times 1 \times 1$ vector. After

this reduction, averaging is performed to obtain the prediction value as output.

3. Results

To validate the effectiveness of the proposed method, we measured nine human intestinal tissue slices. For each tissue section, we selected 50 regions for MM polarimetric imaging and additionally different 50 regions for bright-field imaging. Note that the regions used for MM polarimetric imaging did not overlap with those used for bright-field imaging. We acquired the original polarization images dataset and original bright-field images dataset, both consisted of 450 images, each with a resolution of 1440×1080 pixels. Then, each polarization image and bright-field image were cropped into 30 patches of 256×256 pixels with a certain level of pixel overlap, resulting in augmented datasets of 13,500 polarization images and 13,500 bright-field images. The experiments were conducted on a desktop

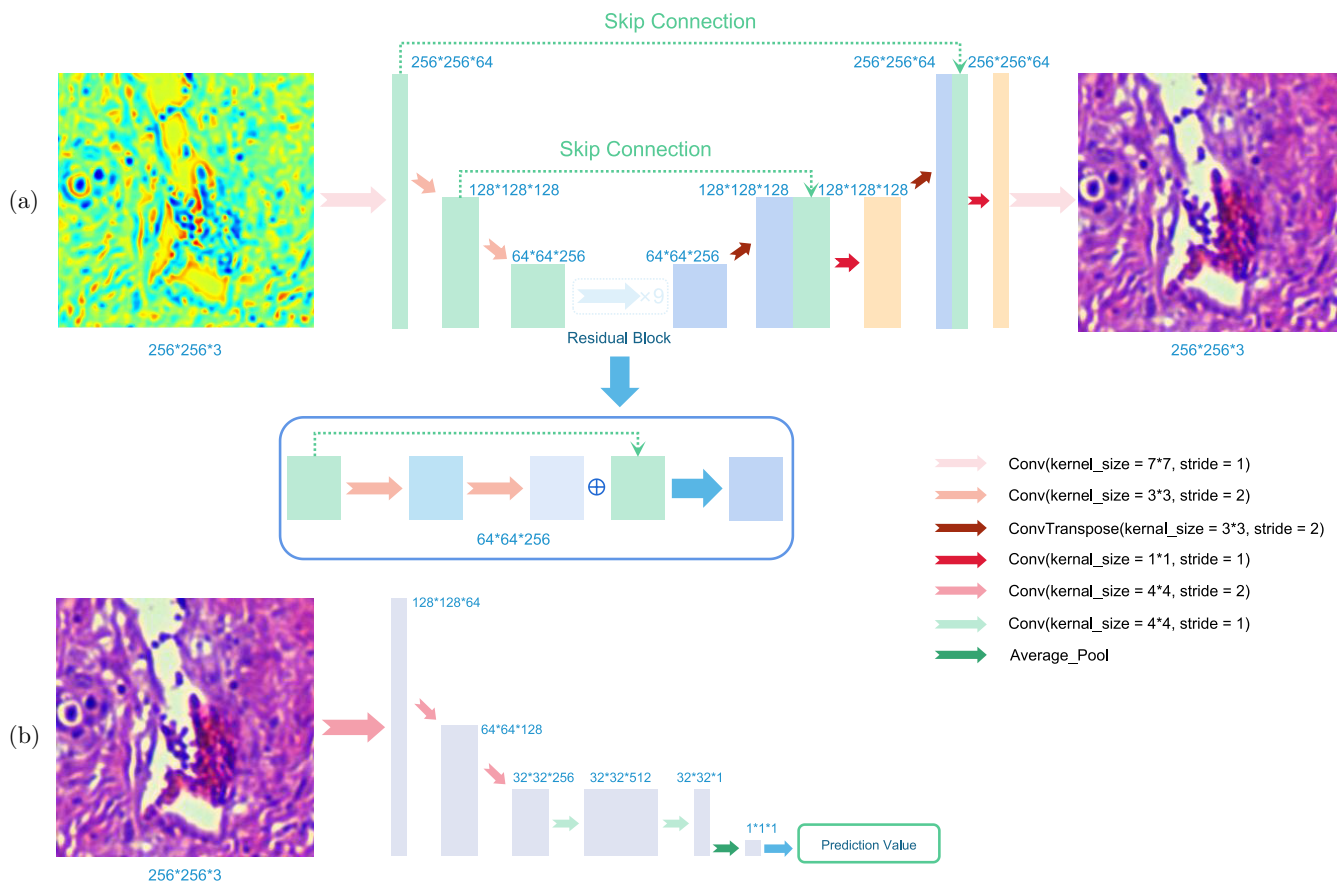


Fig. 3. Architecture of (a) Generator; (b) Discriminator.

computer equipped with a GeForce GTX 3090 GPU. The model was trained in a Python 3.10.0 environment using PyTorch 2.0.1.

Before initiating the model training, we conducted the image normalization, setting the mean and standard deviation of all three image channels to (0.5, 0.5, 0.5). The purpose of such a normalizing is to enhance the model’s generalization capabilities, making it more robust to new data.³⁹ Throughout the model training process, we set various hyperparameters, as indicated in Table 1. The model was trained for a total of 200 epochs, with a batch size of 8. We utilized the Adam optimizer⁴⁰ with an initial learning rate of 0.0002, and the betas parameter representing the exponential decay rates for the momentum and second-moment estimates was set to (0.5, 0.999).⁴¹ Additionally, a learning rate scheduler was implemented to adaptively adjust the optimizer’s learning rate during training. We employed an exponential decay learning rate, where an exponential factor that diminishes as the number of iterations increases was used. This allowed for a larger learning rate in the initial stages to expedite convergence and a smaller learning rate in the later stages to ensure model stability. The decay rate λ was set to 0.9, and the decay period T was defined as 100 epochs.

Furthermore, we integrated a replay buffer mechanism into our training process.⁴² This involved creating a replay buffer to store images generated by the generator within a certain recent timeframe. During the training of the discriminator, there was a 50% chance of randomly selecting previously stored images from the replay buffer as input for the discriminator. This mechanism effectively mitigated oscillations during model training.

While the goal of this study is to train the CycleGAN model using unpaired images, to test the model’s generative performance, a certain amount of paired images were still needed. We selected three regions from each of the nine human intestinal tissue slices we used. Note that these three regions

were different from the previously selected ones. We performed both MM polarization imaging and bright-field imaging on these selected regions, obtaining three pairs of polarization and bright-field images from the same regions for each of the nine human intestinal tissue slices. The pixel numbers in these selected typical regions are sufficient to test the performance of the CycleGAN model. Despite our rigorous efforts to closely align the imaging regions for both modalities, variations in imaging equipment and techniques resulted in imperfect image registration. Consequently, to ensure accurate performance testing of the model, additional registration between these image pairs was necessary.

We employed the Oriented FAST and Rotated BRIEF (ORB) algorithm for the registration of bright-field and polarization images pairs.⁴³ The ORB algorithm is a computer vision technique used for feature detection and description. It combines the Features from Accelerated Segment Test (FAST) keypoint detection algorithm⁴⁴ with Binary Robust Independent Elementary Features (BRIEF) descriptors,⁴⁵ making it a fast and robust feature extraction algorithm. Following the image registration process, we conducted tests on the generative performance of the CycleGAN model. Figure 4 displays the model’s generated results. By comparing the images generated by the model with real bright-field images shown as Fig. 4(b), we can observe that the model could effectively perform the transformation from polarized images to bright-field images. Furthermore, when comparing the results of the model with and without adopting skip-connection structures and SSIM loss functions shown in Figs. 4(c) and 4(d), evidently the former preserved the structural information of images better. Also, it can be noticed that discrepancies in the coloration of structures exist as indicated by the red boxes in Fig. 4.

More specifically, in the bright-field image of H&E-stained slice shown in Fig. 4(b), a structure highlighted in the red box appeared with a purple hue. However, in Fig. 4(c) this structure was virtually stained with a reddish hue, not consistent with the real result. Upon the integration of skip-connection structures and SSIM loss functions, as depicted in Fig. 4(d), the structure was virtually colored with a correct purple hue. This indicated that the model, enhanced with these additional optimization functions, exhibited improved learning

Table 1. Training hyperparameters.

Parameter	Value
epochs	200
batch_size	8
optimizer	Adam, lr = 0.0002, betas = (0.5, 0.999)
lr_scheduler	lambdaLR, $\lambda = 0.9$, $T = 100$

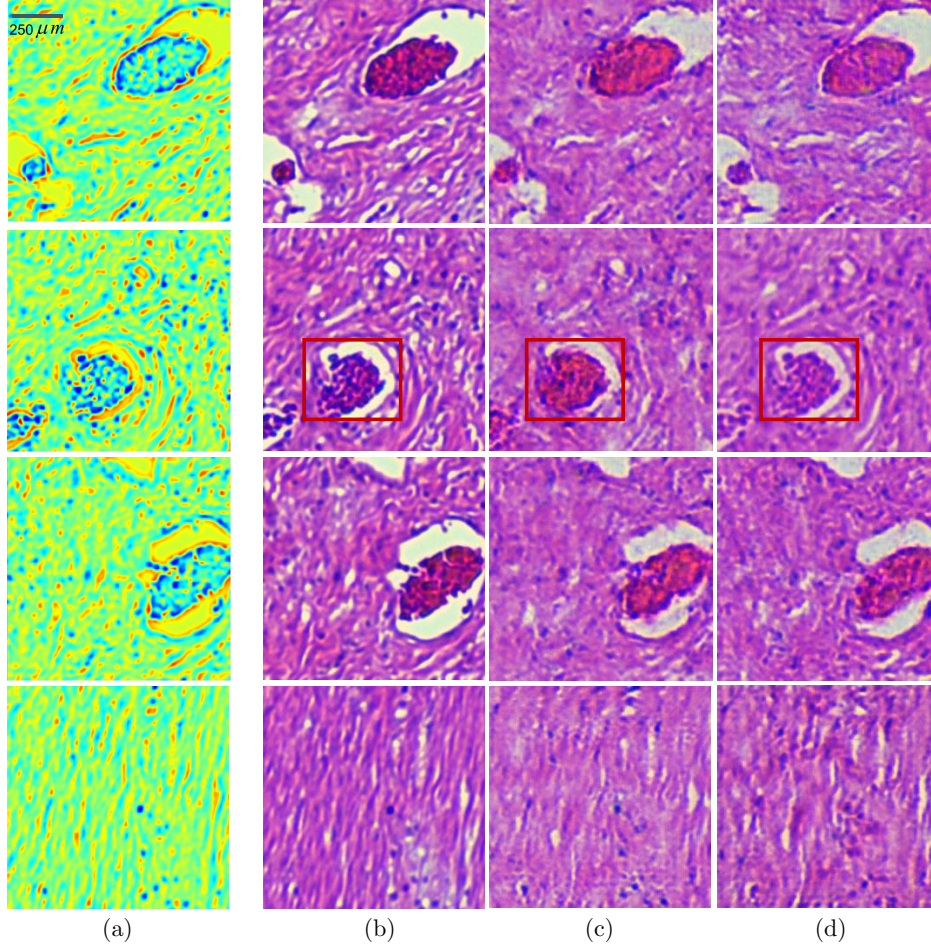


Fig. 4. Testing results of the proposed CycleGAN model. (a) Polarization images as input of the model. (b) Bright-field images registered with polarization images. (c) Generation results of the model without skip-connection structure and SSIM loss function. (d) Generation results of the model with skip-connection structure and SSIM loss function.

capabilities in replicating the staining outcomes of diverse structures.

To further quantitatively evaluate the performance of the proposed model, we utilized two image similarity assessment metrics: Structure Similarity Index Measure (SSIM)⁴⁶ and Peak Signal-to-Noise Ratio (PSNR)⁴⁷ for the assessment. Here, SSIM takes into account aspects such as brightness, contrast, and structure to comprehensively measure the similarity between two images. Its formula is represented by the following equation:

$$\text{SSIM}(x, y) = \frac{(2\mu_x\mu_y + c_1)(\sigma_{xy} + c_2)}{(\mu_x^2 + \mu_y^2 + c_1)(\sigma_x^2 + \sigma_y^2 + c_2)}, \quad (10)$$

where μ_x and μ_y denote the average values of x and y , σ_x and σ_y represent the standard deviations of x and y , σ_{xy} signifies the covariance between x and y , c_1 and c_2 are constants designed to prevent calculation errors caused by a zero denominator.

The calculated SSIM is a value between 0 and 1, where a value closer to 1 indicates a higher degree of similarity between the two images. PSNR, on the other hand, considers the differences between the pixel values of two images. Its calculation is defined by the following equation:

$$\text{PSNR} = 10\log_{10}\left(\frac{\text{MAX}_I^2}{\text{MSE}}\right), \quad (11)$$

where MAX_I denotes the maximum pixel value, and MSE is computed as depicted in the following equation:

$$\text{MSE} = \frac{1}{mn} \sum_{i=0}^{m-1} \sum_{j=0}^{n-1} \|I(i, j) - K(i, j)\|^2 \quad (12)$$

with m and n representing the width and height of the images, and I and K corresponding to the pixel values at the corresponding positions in the two images.

Table 2. Evaluation results of model performance.

	SSIM	PSNR
<i>A</i>	0.63	29.46
<i>A + B</i>	0.69	30.53
<i>A + C</i>	0.66	30.16
<i>A + B + C</i>	0.71	31.24

We conducted ablation experiments to analyze the model's performance, and the testing results are presented in Table 2.

In Table 2, “*A*” represents the model without skip-connection and SSIM loss function, “*B*” represents the model with skip-connection, and “*C*” represents the model with SSIM loss function. It is evident that the inclusion of both skip-connection and the SSIM loss function enhances the model's performance, with the best performance observed when both optimizations *A+B+C* are incorporated, whose SSIM reached 0.71, and PSNR reached 31.24. These results validate the feasibility of training a CycleGAN using unpaired H&E polarization images and bright-field images.

4. Discussion

It should be noted there are still several issues that should be further improved. For instance, the accuracy and contrast of structural information in the images generated by the model can be enhanced further. We utilized polarization data obtained through MM dimensionality reduction after polarization imaging. However, individual MM elements lack clear physical interpretations, and many studies have derived polarization parameters from MM to characterize the polarization properties of samples. These MM derived parameters offer better representational capabilities for sample structure compared to individual MM elements. In future work, it can be considered using combinations of MM derived polarization parameters as inputs to the model to achieve improved results.

5. Conclusions

In this study, we developed a model using unpaired MM polarization images and bright-field images for generating standard H&E-stained tissue images. We separately obtained the unpaired MM

polarization images and bright-field images of human intestinal tissue sections. After obtaining the raw images data, we conducted dimensionality reduction on the MM polarization images and stain normalization on the bright-field images, along with image cropping to augment the dataset, to provide a high-quality dataset for the CycleGAN model training. Then, we selected several regions in the samples for both polarization and bright-field imaging. Image registration algorithms were applied to align the polarization and bright-field images, utilized for evaluating the model's performance. Compared with the existing polarization virtual staining techniques primarily based on the model training with paired images, the proposed CycleGAN-based model simplifies data acquisition and data preprocessing. The testing results demonstrated the feasibility of training CycleGAN with unpaired polarization images and their corresponding bright-field images as a viable approach.


Acknowledgments


Shenzhen Key Fundamental Research Project (No. JCYJ20210324120012035). Chao He would like to thank the support of the Junior Research Fellowship from St John's College, University of Oxford.



Conflicts of Interest

The authors declare that there are no conflicts of interest related to this paper.

ORCID

Jiahao Fan  <https://orcid.org/0009-0005-9071-7914>

Honghui He  <https://orcid.org/0000-0001-7369-7433>

Chao He  <https://orcid.org/0000-0001-9654-830X>
Hui Ma  <https://orcid.org/0000-0001-9662-0447>

References

1. C. He, H. He, J. Chang, B. Chen, H. Ma, M. J. Booth, “Polarisation optics for biomedical and clinical applications: A review,” *Light: Sci. Appl.* **10**(1), 194 (2021).

2. N. Ghosh, I. A. Vitkin, "Tissue polarimetry: Concepts, challenges, applications, and outlook," *J. Biomed. Opt.* **16**(11), 110801 (2011).
3. H. He, R. Liao, N. Zeng, P. Li, Z. Chen, X. Liu, H. Ma, "Mueller matrix polarimetry — an emerging new tool for characterizing the microstructural feature of complex biological specimen," *J. Lightwave Technol.* **37**(11), 2534–2548 (2018).
4. J. Qi, D. S. Elson, "Mueller polarimetric imaging for surgical and diagnostic applications: A review," *J. Biophotonics* **10**(8), 950–982 (2017).
5. J. C. Ramella-Roman, I. Saytashev, M. Piccini, "A review of polarization-based imaging technologies for clinical and preclinical applications," *J. Opt.* **22**(12), 123001 (2020).
6. V. V. Tuchin, "Polarized light interaction with tissues," *J. Biomed. Opt.* **21**(7), 071114 (2016).
7. C. He, J. Chang, P. S. Salter *et al.*, "Revealing complex optical phenomena through vectorial metrics," *Adv. Photonics* **4**(2), 026001 (2022).
8. Y. Shen, R. Huang, H. He, S. Liu, Y. Dong, J. Wu, H. Ma, "Comparative study of the influence of imaging resolution on linear retardance parameters derived from the mueller matrix," *Biomed. Opt. Express* **12**(1), 211–225 (2021).
9. W. E. Baylis, J. Bonenfant, J. Derbyshire, J. Huschilt, "Light polarization: A geometricalgebra approach," *Am. J. Phys.* **61**(6), 534–545 (1993).
10. H. Jerrard, "Modern description of polarized light: Matrix methods," *Opt. Laser Technol.* **14**(6), 309–319 (1982).
11. D. Layden, N. Ghosh, I. A. Vitkin, "Quantitative polarimetry for tissue characterization and diagnosis," *Adv. Biophotonics: Tissue Opt. Sectioning* **5**, 73–108 (2013).
12. Y. Yao, J. Wan, F. Zhang, Y. Dong, L. Chen, H. Ma, "Correlation of image textures of a polarization feature parameter and the microstructures of liver fibrosis tissues," *J. Innov. Opt. Health Sci.* **16**(5), 2241004 (2023).
13. E. Du, H. He, N. Zeng, M. Sun, Y. Guo, J. Wu, S. Liu, H. Ma, "Mueller matrix polarimetry for differentiating characteristic features of cancerous tissues," *J. Biomed. Opt.* **19**(7), 076013 (2014).
14. M. Dubreuil, P. Babilotte, L. Martin, D. Sevrain, S. Rivet, Y. Le Grand, G. Le Brun, B. Turlin, B. Le Jeune, "Mueller matrix polarimetry for improved liver fibrosis diagnosis," *Opt. Lett.* **37**(6), 1061–1063 (2012).
15. C. He, J. Chang, Q. Hu *et al.*, "Complex vectorial optics through gradient index lens cascades," *Nat. Commun.* **10**(1), 4264 (2019).
16. I. Ahmad, M. Ahmad, K. Khan, S. Ashraf, S. Ahmad, M. Ikram, "Ex vivo characterization of normal and adenocarcinoma colon samples by Mueller matrix polarimetry," *J. Biomed. Opt.* **20**(5), 056012 (2015).
17. D. Ivanov, V. Dremine, E. Borisova, A. Bykov, T. Novikova, I. Meglinski, R. Ossikovski, "Polarization and depolarization metrics as optical markers in support to histopathology of ex vivo colon tissue," *Biomed. Opt. Express* **12**(7), 4560–4572 (2021).
18. T. Liu, M. Lu, B. Chen, Q. Zhong, J. Li, H. He, H. Mao, H. Ma, "Distinguishing structural features between crohn's disease and gastrointestinal luminal tuberculosis using Mueller matrix derived parameters," *J. Biophotonics* **12**(12), e201900151 (2019).
19. T. Novikova, A. Pierangelo, S. Manhas, A. Benali, P. Validire, B. Gayet, A. De Martino, "The origins of polarimetric image contrast between healthy and cancerous human colon tissue," *Appl. Phys. Lett.* **102**, 241103 (2013).
20. A. Pierangelo, S. Manhas, A. Benali, C. Fallet, J. L. Totobenazara, M. R. Antonelli, T. Novikova, B. Gayet, A. De Martino, P. Validire, "Multispectral Mueller polarimetric imaging detecting residual cancer and cancer regression after neoadjuvant treatment for colorectal carcinomas," *J. Biomed. Opt.* **18**(4), 046014 (2013).
21. A. Pierangelo, A. Nazac, A. Benali, P. Validire, H. Cohen, T. Novikova, B. H. Ibrahim, S. Manhas, C. Fallet, M. R. Antonelli, "Polarimetric imaging of uterine cervix: A case study," *Opt. Express* **21**(12), 14120–14130 (2013).
22. Y. Wang, H. He, J. Chang, N. Zeng, S. Liu, M. Li, H. Ma, "Differentiating characteristic microstructural features of cancerous tissues using Mueller matrix microscope," *Micron* **79**, 8–15 (2015).
23. L. Deng, C. Chen, W. Yu, C. Shao, Z. Shen, Y. Wang, C. He, H. Li, Z. Liu, H. He, "Influence of hematoxylin and eosin staining on linear birefringence measurement of fibrous tissue structures in polarization microscopy," *J. Biomed. Opt.* **28**(10), 102909 (2023).
24. B. Bai, X. Yang, Y. Li, Y. Zhang, N. Pillar, A. Ozcan, "Deep learning-enabled virtual histological staining of biological samples," *Light: Sci. Appl.* **12**(1), 57 (2023).
25. Y. Rivenson, H. Wang, Z. Wei, K. de Haan, Y. Zhang, Y. Wu, H. Günaydin, J. E. Zuckerman, T. Chong, A. E. Sisk, "Virtual histological staining of unlabelled tissue-autofluorescence images via deep learning," *Nat. Biomed. Eng.* **3**(6), 466–477 (2019).
26. Y. Rivenson, T. Liu, Z. Wei, Y. Zhang, K. de Haan, A. Ozcan, "Phasestain: The digital staining of label-free quantitative phase microscopy images using deep learning," *Light: Sci. Appl.* **8**(1), 23 (2019).

27. L. Si, N. Li, T. Huang, S. Du, Y. Dong, Y. Yao, H. Ma, "Computational image translation from Mueller matrix polarimetry to bright-field microscopy," *J. Biophotonics* **15**(3), e202100242 (2022).
28. D. B. Chenault, J. L. Pezzaniti, R. A. Chipman, "Mueller matrix algorithms," *Proc. SPIE* **1746**, 231–246 (1992).
29. J. Zhou, H. He, Z. Chen, Y. Wang, H. Ma, "Modulus design multiwavelength polarization microscope for transmission Mueller matrix imaging," *J. Biomed. Opt.* **23**(1), 016007 (2018).
30. T. Xuan, H. Zhai, H. He, C. He, S. Liu, H. Ma, "Self-registration of constant-step rotating Mueller matrix polarimeters," *Opt. Lett.* **47**(22), 5797–5800 (2022).
31. L. E. Brouwer, "Beweis der invarianz des n-dimensionalen gebiets," *Math. Ann.* **71**, 305–313 (1911).
32. R. Bro, A. K. Smilde, "Principal component analysis," *Anal. Methods* **6**(9), 2812–2831 (2014).
33. T. A. A. Tosta, P. R. de Faria, L. A. Neves, M. Z. Nascimento, "Computational normalization of H&E-stained histological images: Progress, challenges and future potential," *Artif. Intell. Med.* **95**, 118–132 (2019).
34. A. Vahadane, T. Peng, A. Sethi, S. Albarqouni, L. Wang, M. Baust, K. Steiger, A. M. Schlitter, I. Esposito, N. Navab, "Structure-preserving color normalization and sparse stain separation for histological images," *IEEE Trans. Med. Imag.* **35**(8), 1962–1971 (2016).
35. J. Y. Zhu, T. Park, P. Isola, A. A. Efros, Unpaired image-to-image translation using cycle-consistent adversarial networks, *Proc. IEEE Int. Conf. Computer Vision*, Venice Italy, pp. 2223–2232 (2017).
36. H. Zhao, O. Gallo, I. Frosio, J. Kautz, Loss functions for neural networks for image processing, arXiv:1511.08861.
37. S. Kolhar, J. Jagtap, "Convolutional neural network based encoder-decoder architectures for semantic segmentation of plants," *Ecol. Inform.* **64**, 101373 (2021).
38. T. Tong, G. Li, X. Liu, Q. Gao, Image super-resolution using dense skip connections, *Proc. IEEE Int. Conf. Computer Vision*, Venice, Italy, pp. 4799–4807 (2017).
39. Y. Chen, H. Jiang, C. Li, X. Jia, P. Ghamisi, "Deep feature extraction and classification of hyperspectral images based on convolutional neural networks," *IEEE Trans. Geosci. Remote Sens.* **54**(10), 6232–6251 (2016).
40. S. Bock, M. Weiß, A proof of local convergence for the adam optimizer, *2019 Int. Joint Conf. Neural Networks*, Budapest, Hungary, pp. 1–8 (2019).
41. N. Shazeer, M. Stern, "Adafactor: Adaptive learning rates with sublinear memory cost," *Int. Conf. Machine Learning*, Stockholm, Sweden, pp. 4596–4604 (2018).
42. B. Eysenbach, R. R. Salakhutdinov, S. Levine, "Search on the replay buffer: Bridging planning and reinforcement learning," *Adv. Neural Inf. Process. Syst.* **32**, 15246–15257 (2019).
43. E. Karami, S. Prasad, M. Shehata, Image matching using sift, surf, brief and orb: Performance comparison for distorted images, arXiv:1710.02726.
44. Y. Biadgie, K.-A. Sohn, Feature detector using adaptive accelerated segment test, *2014 Int. Conf. Information Science and Applications*, Seoul, Korea (South), pp. 1–4 (2014).
45. M. Calonder, V. Lepetit, C. Strecha, P. Fua, Brief: Binary robust independent elementary features, *Computer Vision — ECCV 2010: 11th European Conf. Computer Vision*, Heraklion, Crete, Greece, 5–11 September 2010, Proceedings, Part IV 11, Crete, Greece, pp. 778–792 (2010).
46. M. P. Sampat, Z. Wang, S. Gupta, A. C. Bovik, M. K. Markey, "Complex wavelet structural similarity: A new image similarity index," *IEEE Trans. Image Process.* **18**(11), 2385–2401 (2009).
47. J. Korhonen, J. You, "Peak signal-to-noise ratio revisited: Is simple beautiful?" *2012 Fourth Int. Workshop on Quality of Multimedia Experience*, Melbourne, Australia, pp. 37–38 (2012).